Study on Crack Growth Resulting from Spacing and Alignment of Two Circular Holes: A Phase Field Approach

Sayahdin ALFAT

Physics Education Department, Halu Oleo University, Kendari, Southeast Sulawesi, Indonesia; e-mail: sayahdin.alfat@yahoo.com

This study investigates the effects of spacing and alignment between two circular holes on crack growth simulation. Key aspects analyzed include: (a) crack growth behavior, (b) von Mises stress distribution, and (c) energy profiles, all through variations in the spacing and alignment of the holes. The material is assumed to be homogeneous and isotropic, with the following non-dimensional properties: Young's modulus $E = 70$, Poisson's ratio $\nu = 0.35$, and energy release rate $\gamma = 0.5$, which correspond to the real values $E = 70$ GPa, $\nu = 0.35$, and $\gamma = 2800$ J $\cdot$ m^{-2}. Additionally, the body force is neglected ($f(x,t) = 0$). The numerical method used in this research is the adaptive finite element method, which is considered highly robust for solving the phase field model for crack growth. Notable findings include: (a) spacing between the two holes did not significantly alter the crack path, while alignment differences had a significant impact; (b) during the cracking process, the highest stress occurs at the crack tip and the lowest at the crack center; and (c) the time for cracking in materials with two holes varies with spacing and alignment, and elastic and surface energy curves help predict total damage.

Keywords: phase field model, crack path; stress distribution; spacing and alignment of two holes.

1. INTRODUCTION

In the area of fracture mechanics, two factors accelerate crack growth in materials: external and internal factors. Several external factors include external forces that cause overloading [1], thermal injection [2, 3], fluid injection or hydraulic fracturing [4], and hydrogen embrittlement [5–7]. On the other hand, internal factors include properties such as yield and ultimate strengths, Young's modulus, and Poisson's ratio. In other researches [8, 9], the geometrical effects have been shown to influence crack growth acceleration.

Besides the length, width, and thickness of a material, the small-hole effect is a significant part of the geometrical effect that greatly contributes to changes in shape and accelerates the occurrence of cracks in a material [10]. In the investigation of crack propagation in porous materials, some observations have been made: (a) the more holes present in the material, the faster the damage occurs [11], and (b) the spacing and alignment between two circular holes greatly influence crack propagation behavior [12]. Experimentally, investigations of the small-hole effect have been conducted extensively [11–13]. However, these studies do not clearly and fully address the crack propagation process. Specifically, they do not provide visualization of stress distribution at any point, which is a serious issue that needs to be addressed. Therefore, alternative methods for studying this phenomenon are warranted.

One approach that is very suitable and realistic for addressing this problem is the numerical method. Several methods are well-known, highly suitable, and frequently referenced by researchers for investigating crack propagation. These include the finite difference method (FDM) [14, 15], finite element method (FEM) [7, 9, 16, 17], extended finite element method (XFEM) [18–20], discrete element method (DEM) [21, 22], boundary element method (BEM) [23, 24], and meshless/meshfree methods [25–27].

The main objective of crack growth investigation is to track the failure evolution after loading. In the engineering field, numerical investigations are carried out in two ways [28], as follows: first, surface cracking is treated as a discrete discontinuity, as pioneered by Moës et $al.$ [19]. This approach is complicated to apply in three-dimensional cases with branching cracks [29]. Second, surface cracking is modeled using a phase field model (PFM), where the variable z is considered the damage variable ranging between $0 \leq z \leq 1$. In this model, the cracked area is represented by $z = 1$ and the uncracked area by $z = 0$. This method is based on the work of Bourdin et $al.$ [17], Karma et $al.$ [30], Miehe et $al.$ [29], and Kimura et $al.$ [7, 16]. Unlike the first approach, the PFM is considered an alternative and powerful method [7, 16]. Additionally, this approach adapts the Francfort–Marigo model [31] and Ambrosio–Tortorelli regularization [32].

The objectives of this study are to numerically investigate the crack growth behavior under the influence of two holes in homogeneous and isotropic materials using a phase field model (PFM) and to visualize the stress distribution at each time increment. Additionally, elasticity energy, and surface energy profiles will be presented. In this study, the author defines the small holes as circles with a constant diameter while varying the spacing and alignment of the two holes. The study is based on the crack propagation model proposed by Kimura et $al.$ [7, 16].

This article consists of five sections. In Sec. 2, the author presents the crack propagation model proposed by Takaishi–Kimura. Additionally, this section shows

the numerical assumptions, the computational setup, and the physical parameters used. Section 3 details the numerical scheme employed in the simulation. For this purpose, the author utilizes the open-source software FreeFEM++ [33] with the adaptive finite element method (AFEM) as the numerical approach. In Sec. 4, numerical results are presented, including crack propagation behavior in 2D and the effects of spacing and alignment between two circular holes. Finally, Sec. 5 serves as the conclusion, summarizing the findings and outlining future work.

2. CRACK GROWTH MODEL

2.1. The governing equation

In the numerical simulation of crack growth, this research employs a partial differential equation (PDE) model proposed by Takaishi–Kimura [7, 16]. The model is based on the Fracfort–Marigo energy formulation [31]. Let $x = [x_1, x_2]^T \in \Omega \subset \mathbb{R}^2$ denote the position within a solid body characterized by linear elasticity. The displacement is denoted as $u(x,t) = [u_1, u_2]^T \in \mathbb{R}^2$. The boundary of Ω is denoted by Γ, which is divided into Γ_D and Γ_N (see Fig. 1).
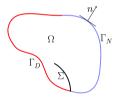

FIG. 1. Illustration of a solid body Ω with an initial crack Σ. Here, Σ is represented by z.

The governing equation for crack growth is as follows:

$$\begin{cases} -\operatorname{div}(\sigma_z[u]) = f(x,t) & \text{in} \quad \Omega \times [0,t], \\ \alpha \dfrac{\partial z}{\partial t} = \left(\epsilon \operatorname{div}(\gamma(x)\nabla z) - \dfrac{\gamma(x)}{\epsilon} z + \sigma[u] : e[u](1-z) \right)_+ & \text{in} \quad \Omega \times [0,t], \end{cases} \quad (1)$$

where z, $f(x,t)$, $\gamma(x)$, and t represent the PFM function for the crack shape [-], the body force [N·m^{-3}], the critical energy release rate [Pa·m], and the time simulation [s], respectively. Meanwhile, α [Pa·s] and ϵ [m] are PFM parameters. Here, $\sigma_z[u] = (1-z)^2\sigma[u]$ is the damage stress tensor [Pa]. Since the material exhibits linear elasticity, its stress tensor is given by $\sigma[u] = \lambda(\nabla \cdot u)I + 2\mu e[u]$, where λ and μ are the Lamé constants [Pa]. The strain tensor $e[u]$ is define as:

$$e[u] = (e_{ij}[u]) \in \mathbb{R}^{d \times d}_{\text{sym}},$$

$$\text{with} \quad e_{ij}[u] = \begin{pmatrix} \dfrac{\partial u_1}{\partial x_1} & \dfrac{1}{2}\left(\dfrac{\partial u_1}{\partial x_2} + \dfrac{\partial u_2}{\partial x_1}\right) \\ \dfrac{1}{2}\left(\dfrac{\partial u_2}{\partial x_1} + \dfrac{\partial u_1}{\partial x_2}\right) & \dfrac{\partial u_2}{\partial x_2} \end{pmatrix}, \quad (2)$$

where $\mathbb{R}^{d \times d}_{\text{sym}}$ is the space of real-valued (symetric) $d \times d$ matrix. In Eq. (1), the boundary and initial conditions are as follows:

$$\begin{cases} u = g(x,t) & \text{on} \quad \Gamma_D \times [0,t], \\ \sigma_z[u]n = q(x,t) & \text{on} \quad \Gamma_N \times [0,t], \\ \dfrac{\partial z}{\partial n} = 0 & \text{on} \quad \Gamma \times [0,t], \\ z|_{t=0} = z_0(x) & \text{in} \quad \Omega, \end{cases} \quad (3)$$

where $g(x,t)$, $q(x,t)$, and n represent the given displacement on Γ_D, the boundary load on Γ_N, and the normal vector, respectively.

In the simulation of crack growth under the effect of two circular holes using homogeneous and isotropic material, several remarks are made: (a) the body force $f(x,t)$ and the boundary load $q(x,t)$ are neglected; (b) the initial cracking is set $z_0(x) = 0$; and (c) while previous research has investigated crack growth in porous or perforated materials numerically [34, 35], the effects of varying the spacing and alignment between two circular holes has not been explored.

2.2. The von Mises stress

Now, we discuss how to visualize stress distribution in a cracking area using the Takaishi–Kimura model [16]. In engineering, this is an enticing prospect, as it allows combining damage distribution with von Mises stress in material loading, as discussed in [36]. To visualize the von Mises stress using the Takaishi–Kimura model, we consider the stress tensor components of the damaged material $\sigma_z[u]$:

$$\sigma_z[u] = \begin{bmatrix} \sigma_{11}^* & \sigma_{12}^* \\ \sigma_{21}^* & \sigma_{22}^* \end{bmatrix},$$

where σ_{11}^*, σ_{22}^*, and $\sigma_{12}^* = \sigma_{21}^*$ satisfy:

$$\sigma_{11}^* = (1-z)^2 \left(\lambda \left(\frac{\partial u_1}{\partial x_1} + \frac{\partial u_2}{\partial x_2} \right) + 2\mu \left(\frac{\partial u_1}{\partial x_1} \right) \right), \quad (4)$$

$$\sigma_{22}^* = (1 - z)^2 \left(\lambda \left(\frac{\partial u_1}{\partial x_1} + \frac{\partial u_2}{\partial x_2} \right) + 2\mu \left(\frac{\partial u_2}{\partial x_2} \right) \right), \tag{5}$$

$$\sigma_{12}^* = (1 - z)^2 \left(\mu \left(\frac{\partial u_2}{\partial x_1} + \frac{\partial u_1}{\partial x_2} \right) \right). \tag{6}$$

Applying Eqs. (4)–(6), the von Mises stress can be modified as follows:

$$\sigma_{vm} = (1 - z)^2 \sqrt{\sigma_{11}^2 - \sigma_{11}\sigma_{22} + \sigma_{22}^2 + 3\sigma_{12}^2}. \tag{7}$$

2.3. System scale

In the present study, the PFM parameters should be set in non-dimensional form for simplicity. Therefore, the author will specifically explain the scaling of Eq. (1) in this section. Let $\widetilde{x} \in \widetilde{\Omega}$ represent the non-dimensional scale of the material:

$$\widetilde{x} = \frac{x}{c_1}, \qquad \widetilde{u} = \frac{u}{c_2}, \qquad \widetilde{C} = \frac{C}{c_3}, \qquad \widetilde{\epsilon} = \frac{\epsilon}{c_1}. \tag{8}$$

Here, x [m], u [m], and C [Pa] are the real parameters for position, displacement, and elastic tensor, respectively. Meanwhile, c_1 [m], c_2 [m], and c_3 [Pa] represent positive scaling constants. By substituting Eq. (8), Eq. (1) can be modified as follows:

$$\begin{cases} -\widetilde{\text{div}} \left((1 - z)^2 \widetilde{\sigma}[\widetilde{u}] \right) = 0 & \text{in} \quad \widetilde{\Omega} \times [0, t], \\[2mm] \widetilde{\alpha} \dfrac{\partial z}{\partial t} = \left(\widetilde{\epsilon} \, \widetilde{\text{div}}(\widetilde{\gamma} \widetilde{\nabla} z) - \dfrac{\widetilde{\gamma}}{\widetilde{\epsilon}} z + \widetilde{\sigma}[\widetilde{u}] : \widetilde{e}[\widetilde{u}](1 - z) \right)_+ & \text{in} \quad \widetilde{\Omega} \times (0, t], \\[2mm] \widetilde{u} = g(\widetilde{x}, t) & \text{on} \quad \Gamma_D \times [0, t], \\[2mm] \widetilde{\sigma}_z[\widetilde{u}] n = q(\widetilde{x}, t) & \text{on} \quad \Gamma_N \times [0, t], \\[2mm] \dfrac{\partial z}{\partial n} = 0 & \text{on} \quad \Gamma \times [0, t], \\[2mm] z|_{t=0} = z_0(\widetilde{x}) & \text{in} \quad \widetilde{\Omega}, \end{cases} \tag{9}$$

where

$$\widetilde{\alpha} = \frac{c_1^2}{c_3 c_2^2} \alpha, \quad \widetilde{\gamma} = \frac{c_1}{c_3 c_2^2} \gamma, \quad \widetilde{\sigma}[\widetilde{u}] = \frac{c_1}{c_3 c_2} \sigma[u], \quad \widetilde{e}[\widetilde{u}] = \frac{c_1}{c_2} e[u].$$

For the von Mises stress in Eq. (7), it is modified as follows:

$$\sigma_{vm} = \frac{c_2 c_3}{c_1} \widetilde{\sigma}_{vm}. \tag{10}$$

As a remark, Eq. (10) is applied to calculate the von Mises stress in the numerical example. Hereafter we will omit the symbol "$\sim$" in Eq. (9) for simplicity. In the present study, we choose the approximation for the positive scaling constants for simplicity: $c_1 = 5 \times 10^{-3}$ m, $c_2 = 2 \times 10^{-4}$ m, and $c_3 = 1 \times 10^9$ Pa.

2.4. The computational setup and physical parameters

Our research aims to numerically investigate the crack growth behavior due to the effects of spacing and alignment between two circular holes by varying their configuration. Therefore, specific values for the spacing and alignment between the two circular holes are detailed in Table 1. Meanwhile, our computational domain is originally set as a rectangle with dimensions $[0.0, 2.0] \times [0.0, 2.0]$, and the hole geometry is circular with a uniform diameter of 0.1 (see Fig. 2).

TABLE 1. Illustration of spacing and alignment of two circular holes.

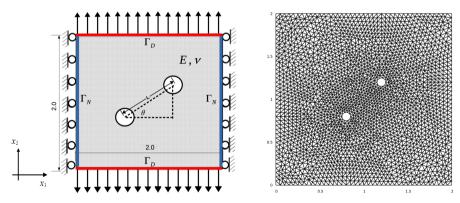| Case	Alignments of two holes θ	Spacing between two circular holes L		
		0.2	0.4	0.6
Case I	$0°$ inclined holes	$\checkmark$	$\checkmark$	$\checkmark$
Case II	$45°$ inclined holes	$\checkmark$	$\checkmark$	$\checkmark$
Case III	$90°$ inclined holes	$\checkmark$	$\checkmark$	$\checkmark$

FIG. 2. Domain setup (left) and illustration of the computational domain with grid after non-dimensional scaling (right). In the left figure, the red and blue lines represent the boundaries for Γ_D and Γ_N, respectively.

In the following numerical simulations, the material properties are: Young's modulus $E = 70$, Poisson's ratio $\nu = 0.35$, and energy release rate $\gamma = 0.5$. Other parameters of the PFM, such as α and ϵ, are set to $\alpha = 1 \times 10^{-3}$ and $\epsilon = 1 \times 10^{-3}$, respectively. These are all non-dimensional parameters. Based

on the system scale discussed in Subsec. 2.3, these properties correspond to $E = 70$ GPa, $\gamma = 2800$ J·m^{-2}, $\alpha = 1120$ Pa·s, and $\epsilon = 5 \times 10^{-6}$ m.

3. Numerical scheme

To obtain a numerical solution for crack growth as shown in Eq. (9), the author employs AFEM with a semi-implicit scheme. Before proceeding, we will present the weak form of the crack growth – Eq. (9). Let us define the test functions (w, v), $V^u := \{w \in H^1(\Omega) \mid w = 0 \text{ on } \Gamma_D\}$, and $V^z := \{v \in H^1(\Omega) \mid v = 0 \text{ on } \Gamma_N\}$, where $H^1(\Omega)$ is the Sobolev space. Then, we have:

$$a_u(u^k, w) = l_u^k(w) \qquad (\forall w \in V^u),$$

$$a_z(z^k, v) = l_z^k(v) \qquad (\forall v \in V^z),$$

where

$$
\begin{cases}
a_u(u^k, w) := \displaystyle\int_\Omega (1 - z^{k-1})^2 \big(\lambda(\text{div}(u^k))(\text{div}(w)) + 2\mu e[u^k] : e[w]\big) dx, \\
l_u^k(w) \quad := 0,
\end{cases}
\tag{11}
$$

and

$$
\begin{cases}
a_z(z^k, v) := \displaystyle\int_\Omega \left(1 + \frac{\Delta t}{\alpha}\left(\frac{\gamma}{\epsilon} + \big(\lambda(\text{div }(u^{k-1}))^2 + 2\mu(e[u^{k-1}])^2\big)\right)\right) z^k v\, dx \\
\qquad\qquad\qquad\qquad\qquad + \displaystyle\int_\Omega \frac{\epsilon \Delta t}{\alpha}(\gamma \nabla z^k) \cdot \nabla v\, dx, \\
l_z^k(v) \quad := \displaystyle\int_\Omega \frac{\Delta t}{\alpha}\big(\lambda(\text{div }(u^{k-1}))^2 + 2\mu(e[u^{k-1}])^2\big)v\, dx + \int_\Omega z^{k-1} v\, dx.
\end{cases}
\tag{12}
$$

Since we are applying the AFEM to solve Eqs. (11) and (12), we set the minimum mesh size $(h_{\min}) = 1 \times 10^{-3}$ and maximum number of vertices $(nbvx)$ $= 50\,000$. In this study, the time simulation is $t = k\Delta t$ with $k = (0, 1, 2, ...)$ while $\Delta t = 1 \times 10^{-3}$. As a remark, the remeshing process at each time step Δt is based on changes in the z parameter. Equations (11) and (12) are solved using FreeFEM++ [33] with P2 elements.

4. Result and discussion

In this section, we present the numerical results of crack growth using the PFM through FreeFEM++ and ParaView [37], including stress distribution and profiles of elastic and surface energies.

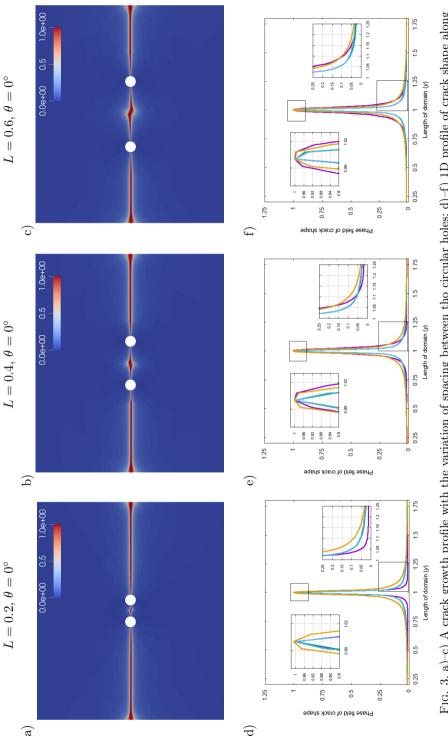## 4.1. Behavior of crack propagation and the von Mises stress profile

The main objective of our study is to demonstrate crack growth behavior under the effect of spacing and alignment between two circular holes. All simulations use $g(x, t) = 5 \times 10^{-3} t$. To illustrate crack propagation behavior, the author divides the study into three sections based on the alignment of the two small holes, as shown in Figs. 3, 6, and 7.
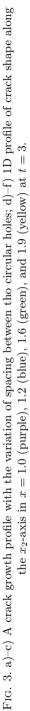
Figures 3a–c visualize crack propagation behavior in material with alignment $\theta = 0°$ and spacing variations of 0.2, 0.4, and 0.6. Generally, applying the alignment $\theta = 0°$ and varying the spacing does not affect the crack propagation behavior. Overall, the resulting cracks propagate straight between the two circular holes. Figure 3 also provides additional information, such as color thickening on both sides of the domain and around the point where the cracks merge. This phenomena indicates that the cracks are larger in these areas or that they enlarge during the growth process (see Figs. 3d–f). In this first case, the most obvious difference is the temporal evolution of stress at points in the material (see Fig. 4a). This shows that the greater the distance between the two holes, the greater the stress. Additionally, the crack propagation process in this case can be divided into three main phases: (a) initially, cracks grow around the two circular holes; (b) they grow straight and connect the two holes; and (c) the material separates into two parts. Since the crack propagation behavior is similar for different values of L, we present the crack profile for $L = 0.4$ only (see Fig. 5).

In the second case, the alignment of the two circular holes at $\theta = 45°$ and the spacing variation exhibited differences in crack growth behavior. As shown in Figs. 6a–c, the increasing distance between the two circular holes generates a curved crack path. Another interesting phenomenon observed in Figs. 6a–c is that the curved crack paths between the two circular holes appear to be connected, but they are not. Additionally, we observe the stress field in the form of von Mises stress in a 2D view. It is evident that the highest stress concentration occurs at the crack tips, with no significant increase in stress in other areas, as shown in Figs. 6d–f. As a remark, this phenomenon occurs in all cases, not just the second; however, we do not show these results here.

Similar to the first case, one striking difference in the second case is the temporal stress evolution. Figure 4b shows that the maximum stress needed to fracture the material varies. Based on Fig. 4b, it can be concluded that the greater the spacing between the two small holes, the greater the stress required.

In the final case, the author applied the alignment $\theta = 90°$ with spacing variations of $L = 0.2, 0.4, 0.6$. In this case, two types of resulting cracks were observed: dominant cracking (large cracks) and minor cracking (small cracks). The dominant cracking tended to grow with the increasing spacing between the
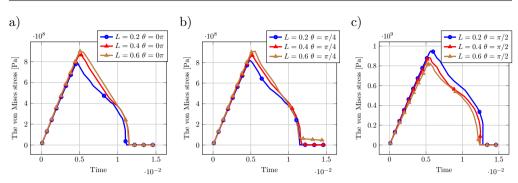
FIG. 3. a)–c) A crack growth profile with the variation of spacing between tho circular holes; d)–f) 1D profile of crack shape along the x_2-axis in $x = 1.0$ (purple), 1.2 (blue), 1.6 (green), and 1.9 (yellow) at $t = 3$.

FIG. 4. Dimensional von Mises stress profiles at point $(1, 0.5)$ with spacing and alignment variations for: a) Case I, b) Case II, and c) Case III, obtained using Eq. (10).
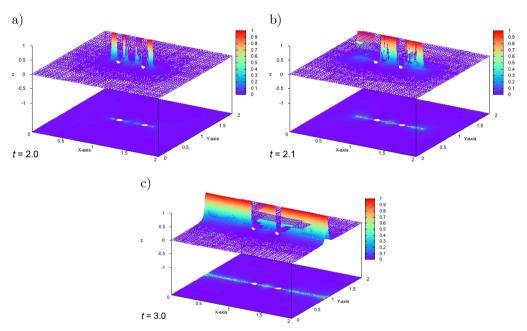

FIG. 5. Crack propagation profile from a bird's-eye view for $L = 0.4$, $\Theta = 0°$ at different times.

two circular holes, while the growth of the minor cracking remained stagnant or constant (see Figs. 7a–c). This phenomenon is caused by the greater stress around the dominant cracking area compared to the minor cracking area (see Figs. 7d–f). As a result, the growth of the dominant cracking is faster. Additionally, the resulting crack type exhibited straight propagation, which is smaller around the small hole and enlarged on both sides of the material. Another noteworthy difference in this case, compared to the previous two cases, is the temporal evolution of the von Mises stress. Here, the smaller the distance between the two circular holes, the higher the maximum stress, and vice versa (see Fig. 4c).
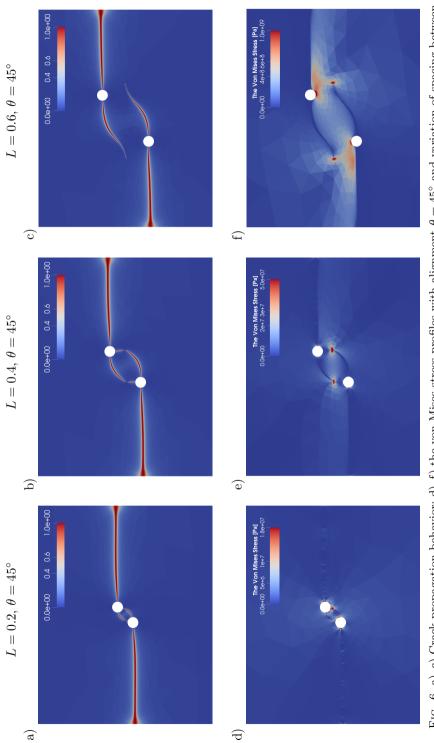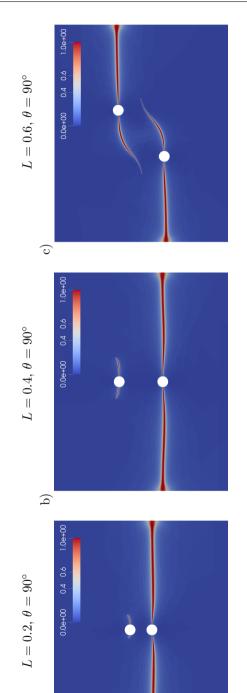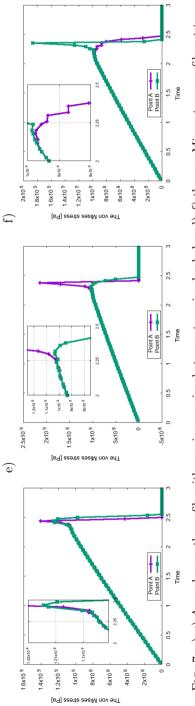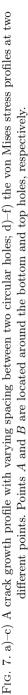
FIG. 6. a)–c) Crack propagation behavior; d)–f) the von Mises stress profiles with alignment $\theta = 45°$ and variation of spacing between two circular holes. The profiles in d)–f) are calculated using Eq. (10).

FIG. 7. a)–c) A crack growth profile with varying spacing between two circular holes; d)–f) the von Mises stress profiles at two different points. Points A and B are located around the bottom and top holes, respectively.

As explained in Sec. 3, our work has applied the AFEM, a type of remeshing technique in FEM. It was considered very suitable for predicting crack paths. Figures 8a and 8b show that the remeshing process occurs only in the cracking area. As the crack grows, the number of vertices increases (see Fig. 8c). The figure illustrates two key points: (a) when the number of vertices increases significantly, crack growth is occurring, and (b) when the number of vertices converges, crack growth has reached its maximum.
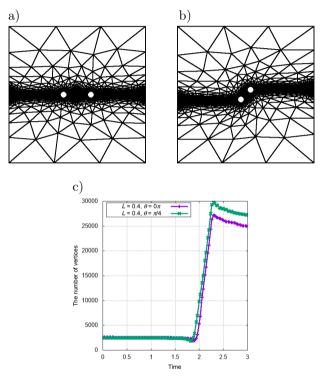

FIG. 8. Crack profiles using AFEM at a) $L = 0.4$, $\theta = 0°$; b) $L = 0.4$, $\theta = 45°$; and c) the evolution number of the vertices.

4.2. Elastic and surface energy

A strong indicator of material failure is the drastic change in elastic and surface energies. According to the Takaishi–Kimura model [16], these energies can be formulated as follows:

$$\mathcal{E}_{el}(u, z) = \frac{1}{2} \int_{\Omega} (1 - z)^2 \sigma[u] : e[u] dx,$$

$$E_s(z) = \frac{1}{2} \int_{\Omega} \gamma \left(\epsilon |\nabla z|^2 + \frac{1}{\epsilon} z^2 \right) dx.$$

Theoretically, a lower maximum elastic energy indicates that a material is more susceptible to cracking, and vice versa [38, 39]. Our results show that the material with a spacing of $L = 0.2$ and an alignment of $\theta = 0°$ is perishable. Conversely, the non-perishable material has a spacing of $L = 0.6$ and an alignment of $\theta = 90°$, as clearly illustrated in Fig. 9a. Specifically, materials with spacings and alignments of $L = 0.6$, $\theta = 0°$, $L = 0.4$, $\theta = 45°$, and $L = 0.6$, $\theta = 45°$ demonstrate similar strength characteristics.
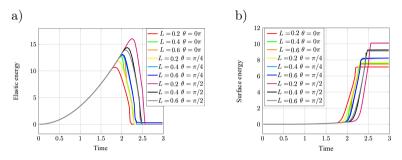

Fig. 9. The non-dimensional profiles for a) elastic and b) surface energies.

An interesting feature of the elastic energy curve is its ability to indicate total material damage (particularly when the material separates into two parts). In our study, all materials were almost completely damaged except for the material with $L = 0.6$, $\theta = 45°$, where the elastic energy did not reach zero until $t = 3$. Additionally, despite variations in the times for initial crack formation leading to total damage, the required times tended to be similar. This was observed in materials with lengths and alignments between two circular holes of $L = 0.4$, $\theta = 0°$, $L = 0.6$, $\theta = 0°$, and $L = 0.2$, $\theta = 45°$, as strongly supported by Fig. 9b. The figure illustrates that the required time to reach convergence was similar across these cases.

5. Conclusions

In this study, a PFM was employed to visualize crack propagation behavior under variations in spacing and alignment between two small holes. Based on the numerical results, several conclusions can be drawn: (a) the spacing between the two circular holes in the material did not significantly change the crack path. In contrast, variations in the alignment of the two small holes significantly impacted the crack path; (b) during the cracking process, the highest stress distribution occurred at the crack tip, while the lowest stress was found at the center of the crack. This is clearly shown in Figs. 6d–f; and (c) the time required for cracking in a material with two holes of varying spacing and align-

ment varies. Furthermore, the elastic energy and surface energy curves can help predicting the extent of total material damage.

The simulation used symmetrically sized materials, which significantly influenced crack propagation behavior. Future studies will require a thorough investigation involving variations in the length and width of the domain to further understand the complexities of crack growth.

References

1. L.P. Borrego, J.M. Ferreira, J.M. Pinho da Cruz, J.M. Costa, Evaluation of overload effects on fatigue crack growth and closure, *Engineering Fracture Mechanics*, **70**(11): 1379–1397, 2003, doi: 10.1016/S0013-7944(02)00119-4.

2. S. Alfat, New Frameworks of PFM for Thermal Fracturing in The Linear Thermoelasticity Solids Based on a Microforce Balance Approach, 19 December 2023, PREPRINT (Ver. 1) available at Research Square, doi: 10.21203/rs.3.rs-3776383/v1.

3. S. Alfat, M. Kimura, A.M. Maulana, Phase field models for thermal fracturing and their variational structures, *Materials*, **15**(7): 2571, 2022, doi: 10.3390/ma15072571.

4. M.K. Hubbert, D.G. Willis, Mechanics of hydraulic fracturing, *Transactions of the AIME*, **210**(01): 153–168, 1957, doi: 10.2118/686-G.

5. T. Takaishi, Phase field crack growth model with hydrogen embrittlement, [in:] *Mathematical Analysis of Continuum Mechanics and Industrial Applications: Proceedings of the International Conference CoMFoS15*, pp. 27–34, Springer, Singapore, 2017.

6. E. Martinez-Paneda, A. Golahmar, C.F. Niordson, A phase field formulation for hydrogen assisted cracking, *Computer Methods in Applied Mechanics and Engineering*, **342**: 742–761, 2018, doi: 10.1016/j.cma.2018.07.021.

7. M. Kimura, T. Takaishi, S. Alfat, T. Nakano, Y. Tanaka, Irreversible phase field models for crack growth in industrial applications: thermal stress, viscoelasticity, hydrogen embrittlement, *SN Applied Sciences*, **3**(9): 781, 2021, doi: 10.1007/s42452-021-04593-6.

8. D. Taylor, Geometrical effects in fatigue: A unifying theoretical model, *International Journal of Fatigue*, **21**(5): 413–420, 1999, doi: 10.1016/S0142-1123(99)00007-9.

9. S. Alfat, M. Kimura, M.Z. Firihu, R. Rahmat, Numerical investigation of shape domain effect to its elasticity and surface energy using adaptive finite element method, [in:] *Metallurgy and Advanced Material Technology for Sustainable Development (ISMM2017)*, 2018, **1964**(1): 020011, doi: 10.1063/1.5038293.

10. H. Haeri, V. Sarfarazi, The effect of micro pore on the characteristics of crack tip plastic zone in concrete, *Computers and Concrete*, **17**(1): 107–127, 2016, doi: 10.12989/cac. 2016.17.1.107.

11. K.S. Churn, D.N. Yoon, Pore formation and its effect on mechanical properties in W–Ni–Fe heavy alloy, *Powder Metallurgy*, **22**(4): 175–178, 1979.

12. X.S. Wang, J.H. Fan, B.S. Wu, Y. Li, Effects of distance and alignment holes on fatigue crack behaviors of cast magnesium alloys, *Advanced Materials Research*, **33**: 13–18, 2008, doi: 10.4028/www.scientific.net/AMR.33-37.13.

13. X.S. Wang, C.H. Tan, J. Ma, X.D. Zhu, Q.Y. Wang, Influence of multi-holes on fatigue behaviors of cast magnesium alloys based on in-situ scanning electron microscope technology, *Materials*, **11**(9): 1700, 2018, doi: 10.3390/ma11091700.

14. Y.M. Chen, Numerical solutions of three dimensional dynamic crack problems and simulation of dynamic fracture phenomena by a "non-standard" finite difference method, *Engineering Fracture Mechanics,* **10**(4): 699–708, 1978, doi: 10.1016/0013-7944(78)90028-0.

15. A. Dorogoy, Finite difference method for solving crack problems in a functionally graded material, *Simulation*, **95**(10): 941–953, 2019, doi: 10.1177/003754971880289.

16. M. Kimura, T. Takaishi, A phase field approach to mathematical modeling of crack propagation, [in:] R. Nishii *et al.* [Eds.], *A Mathematical Approach to Research Problems of Science and Technology. Mathematics for Industry*, Vol. 5, pp. 161–170, Springer, Tokyo, 2014, doi: 10.1007/978-4-431-55060-0_13.

17. B. Bourdin, G.A. Francfort, J.J. Marigo, Numerical experiments in revisited brittle fracture, *Journal of the Mechanics and Physics of Solids*, **48**(4): 797–826, 2000, doi: 10.1016/S0022-5096(99)00028-9.

18. G. Zi, T. Belytschko, New crack-tip elements for XFEM and applications to cohesive cracks, *International Journal for Numerical Methods in Engineering*, **57**(15): 2221–2240, 2003, doi: 10.1002/nme.849.

19. N. Moës, J. Dolbow, T. Belytschko, A finite element method for crack growth without remeshing, *International Journal for Numerical Methods in Engineering*, **46**(1): 131–150, 1999, doi: 10.1002/(SICI)1097-0207(19990910)46:1<131::AID-NME726>3.0.CO;2-J.

20. G.L. Golewski, P. Golewski, T. Sadowski, Numerical modelling crack propagation under Mode II fracture in plain concretes containing siliceous fly-ash additive using XFEM method, *Computational Materials Science*, **62**: 75–78, 2012, doi: 10.1016/j.commat sci.2012.05.009.

21. H. Kim, M.P. Wagoner, W.G. Buttlar, Simulation of fracture behavior in asphalt concrete using a heterogeneous cohesive zone discrete element model, *Journal of Materials in Civil Engineering*, **20**(8): 552–563, 2008, doi: 10.1061/(ASCE)0899-1561(2008)20:8(552).

22. L.U.C. Scholtès, F.V. Donzé, Modelling progressive failure in fractured rock masses using a 3D discrete element method, *International Journal of Rock Mechanics and Mining Sciences*, **52**: 18–30, 2012, doi: 10.1016/j.ijrmms.2012.02.009.

23. Y. Mi, M. Aliabadi, Three-dimensional crack growth simulation using BEM, *Computers & Structures*, **52**(5): 871–878, 1994, doi: 10.1016/0045-7949(94)90072-8.

24. C.S. Chen, E. Pan, B. Amadei, Fracture mechanics analysis of cracked discs of anisotropic rock using the boundary element method, *International Journal of Rock Mechanics and Mining Sciences*, **35**(2): 195–218, 1998.

25. S. Wang, H. Liu, Modeling brittle–ductile failure transition with meshfree method, *International Journal of Impact Engineering*, **37**(7): 783–791, 2010, doi: 10.1016/j.ijimpeng.2010.01.006.

26. B.N. Rao, S. Rahman, An efficient meshless method for fracture analysis of cracks, *Computational Mechanics*, **26**(4): 398–408, 2000, doi: 10.1007/s004660000189.

27. S. Li, W.K. Liu, Meshfree and particle methods and their applications, *Applied Mechanics Review*, **55**(1): 1–34, 2002, doi: 10.1115/1.1431547.

28. B. Giovanardi, A. Scotti, L. Formaggia, A hybrid XFEM–Phase field (Xfield) method for crack propagation in brittle elastic materials, *Computer Methods in Applied Mechanics and Engineering*, **320**: 396–420, 2017, doi: 10.1016/j.cma.2017.03.039.

29. C. Miehe, M. Hofacker, F. Welschinger, A phase field model for rate-independent crack propagation: Robust algorithmic implementation based on operator splits, *Computer Methods in Applied Mechanics and Engineering*, **199**(45–48): 2765–2778, 2010, doi: 10.1016/j.cma.2010.04.011.

30. A. Karma, D.A. Kessler, H. Levine, Phase-field model of mode III dynamic fracture, *Physical Review Letters*, **87**(4): 045501, 2001, doi: 10.1103/PhysRevLett.87.045501.

31. G.A. Francfort, J.-J. Marigo, Revisiting brittle fracture as an energy minimization problem, *Journal of the Mechanics and Physics of Solids*, **46**(8): 1319–1342, 1998, doi: 10.1016/S0022-5096(98)00034-9.

32. L. Ambrosio, V.M. Tortorelli, On the approximation of free discontinuity problems, *Bollettino della Unione Matematica Italiana*, **6**: 105–123, 1992.

33. F. Hecht, New development in FreeFem++, *Journal of Numerical Mathematics*, **20**(3–4): 251–266, 2012, doi: 10.1515/jnum-2012-0013.

34. T.T. Nguyen, J. Yvonnet, Q.-Z. Zhu, M. Bornert, C. Chateau, A phase field method to simulate crack nucleation and propagation in strongly heterogeneous materials from direct imaging of their microstructure, *Engineering Fracture Mechanics*, **139**: 18–39, 2015, doi: 10.1016/j.engfracmech.2015.03.045.

35. P. Chakraborty, P. Sabharwall, M.C. Carroll, A phase-field approach to model multi-axial and microstructure dependent fracture in nuclear grade graphite, *Journal of Nuclear Materials*, **475**: 200–208, 2016, doi: 10.1016/j.jnucmat.2016.04.006.

36. J.G. Londono, L. Berger-Vergiat, H. Waisman, An equivalent stress-gradient regularization model for coupled damage-viscoelasticity, *Computer Methods in Applied Mechanics and Engineering*, **322**: 137–166, 2017, doi: 10.1016/j.cma.2017.04.010.

37. J. Ahrens, B. Geveci, C. Law, *ParaView: An End-User Tool for Large-Data Visualization*, Technical Report, LA-UR-03-1560, Los Alamos National Laboratory, 2005.

38. D.P.H. Hasselman, Elastic energy at fracture and surface energy as design criteria for thermal shock, *Journal of the American Ceramic Society*, **46**(11): 535–540, 1963.

39. E. Orowan, Energy criteria of fracture, *Welding Journal Research Supplement*, **34**: 157–160, 1955.